

RESEARCH

Open Access



# Fabrication of perfect plasmonic absorbers for blue and near-ultraviolet lights using double-layer wire-grid structures

Atsushi Motogaito , Ryoga Tanaka and Kazumasa Hiramatsu

## Abstract

This study proposes using double-layer wire-grid structures to create narrow-band, perfect plasmonic absorbers, which depend on polarization, for the short-wavelength visible and near-ultraviolet regions of the electromagnetic spectrum. A rigorous coupled-wave analysis reveals that the maximum absorption attained using Ag and Al is ~ 90% at 450 and 375 nm. Experiments using Ag yielded results similar to those predicted by simulations. These results demonstrate that narrow-band perfect plasmonic absorbers, which depend on the polarization, can be realized at 450 and 375 nm using Ag or Al.

**Keywords:** Plasmonic filter, Perfect absorber, Wire-grid structure, Propagating surface plasmon, Absorption, Near-UV region

## Introduction

Optical filters are used over the wide wavelength range extending from the ultraviolet (UV) to infrared region of the spectrum. They can be roughly divided by function, such as for improving the brightness and contrast of images, selecting light and color at a specific wavelength by transmission or reflection, or scattering and attenuating light. In this study, we focused on an optical filter for narrow-band wavelength selection. Such filters can be divided into three types: filters that transmit light of a specific wavelength, filters that reflect light, and filters that absorb light. Examples include filters used for biosensing [1], infrared spectroscopy [2], solar cells [3–5], cooling by heat release [6–8], image sensors [9], color filters [10–18], detectors [19–21], and fluorescence observations [22].

In this study, we have focused on perfect absorbers, which are one kind of wavelength-selection filter. Perfect absorbers have been studied for visible, infrared, and THz-light applications [2, 3, 17, 23–26]. On the contrary, UV applications include bandpass filters [27–30], band-stop filters [31], and broad-band absorbers from

the UV to near infrared [32]. However, there are few reports of narrow-band perfect absorbers for the UV. If a perfect absorber of narrow-band UV light can be fabricated, UV light of a specific wavelength can be eliminated almost completely. For example, such an absorber can be used to remove the excitation light from fluorescence observations to enable the detection of only the visible light and obtain a clearer fluorescence image. Such a perfect absorber can not only be fabricated as a multilayer film structure from metal or a dielectric material but can also be produced using a metasurface, plasmonic crystals, metal nanoparticles, photonic crystals, graphene, and other materials [33–36].

Previously, we experimentally demonstrated extraordinary transmission phenomena due to propagating surface-plasmon resonances in a metal diffraction-grating structure [37, 38] and applied this phenomenon to surface-plasmon sensors [39, 40] and polarizing devices [41]. These extraordinary transmission phenomena arise when surface-plasmon resonances propagate over the metal diffraction-grating structure. By exploiting this phenomenon, we obtain the desired absorption characteristics with a simpler structure than a metamaterial by controlling the period and size of the metal diffraction-grating

\* Correspondence: [motogaito@elec.mie-u.ac.jp](mailto:motogaito@elec.mie-u.ac.jp)

Graduate School of Engineering, Mie University, 1577 Kurima-machiya-cho, Tsu, Japan

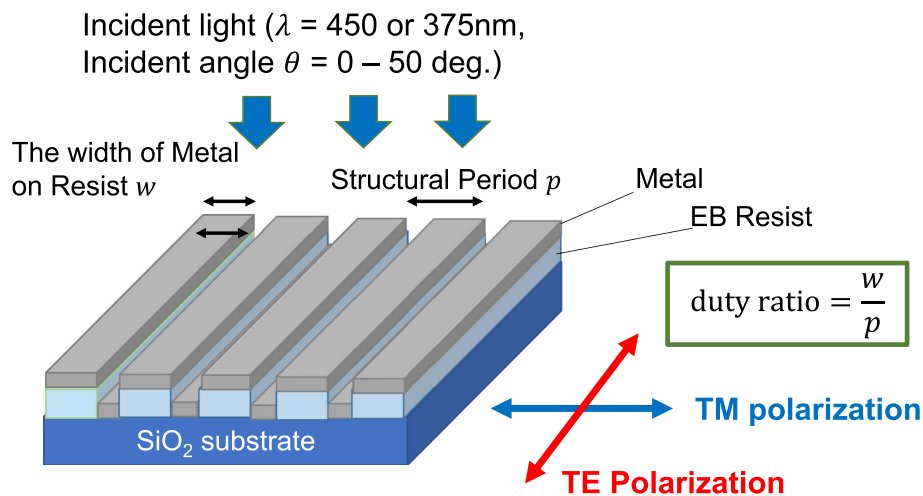


**Fig. 1** Schematic of the wire-grid structure. This structure comprises metal and electron-beam (EB) resist layer on the SiO<sub>2</sub> substrate. Parameters  $p$  and  $w$  are the structural period and the width of metal on the resist layer, respectively.  $w/p$  is the duty ratio of the periodical structure. The parameter  $h$  is the thickness of the EB resist layer. The details of these values are shown in Table 1. The wavelength  $\lambda$  is between 450 and 375 nm. The incident angle  $\theta$  is between 0° and 50°

structure. Further, an absorbance close to 100% can be realized using this extraordinary absorption phenomenon, enabling the creation of a narrow-band perfect absorber for a specific wavelength.

In the present study, we used a double-layer wire-grid structure, which is one type of metal diffraction-grid structure, to absorb p-polarized short-wavelength visible light and near-UV light at a specific wavelength. To produce a narrow-band perfect absorber having a polarization dependence that allows selection of the wavelength and the polarization direction, we fabricated perfect absorbers for the wavelengths 450 and 375 nm and characterized their optical properties.

### Design and simulation

In this study, we performed numerical analyses with the rigorous coupled-wave analysis (RCWA) method using MATLAB (Math Works) software and the program rcwa-1d (Source Forge, <http://rcwa-1d.sourceforge.net/>). A schematic diagram of the two-layer wire-grid structure to be produced is shown in Fig. 1. A diffraction-grating structure with lines and spaces was first prepared on a quartz-glass substrate with an electron-beam (EB) resist, and then Ag or Al was deposited on it. The design parameters are the wavelength of light  $\lambda$ , the angle of incidence  $\theta$ , the grating period  $p$ , the width  $w$  of the resist layer, the duty ratio  $w/p$ , the thickness  $h$  of the resist, and the thickness  $t$  of the metal. Table 1 shows the parameters simulated in this study. The wavelength of the light is 450 nm for the blue laser and 375 nm for the near-UV laser, and we calculated the transmittance, reflectance, and absorbance, depending on the angle of incidence, as well as two kinds of reflectance mappings

while changing the angle of incidence. One type of map is that between the period  $p$ , the angle of incidence  $\theta$ , and the reflectance, while the other is the relationship between the energy  $\hbar\omega$ , the wave number  $k$ , and the reflectance.

### Experimental method

Figure 2 shows the procedure used in fabricating the wire-grid structure. We first cleaned a SiO<sub>2</sub> glass substrate with an organic solvent and then applied hexamethyl disilazane, the EB resist ZEP-520A, and an antistatic agent onto it. Next, we performed EB lithography using an EB lithography system (JEOL, JBX6300SF). The drawing conditions were an accelerating voltage of 100 kV, a beam current of 200 pA, and a dose amount of 200  $\mu\text{C}/\text{cm}^2$ . After drawing the grid pattern, we removed the antistatic agent and then developed the resist. Next, we deposited Ag using a DC magnetron-sputtering device (SANYU, SC-701Mk-II) to form a double-layer wire-grid structure. The advantage of using this procedure is that the lift-off process can be omitted, and the wire-grid structure can be produced easily.

**Table 1** Simulation and fabrication conditions of the wire-grid structures

Wavelength $\lambda$ (nm)	450		375	
	Ag	Al	Ag	Al
Period $p$ (nm)	350	350	350	350
Width of resist $w$ (nm)	262.5	122.5	182.0	287.0
Duty ratio $w/p$	0.75	0.35	0.52	0.82
Thickness of resist $h$ (nm)	100	100	100	100
Thickness of metal $t$ (nm)	80	80	100	100

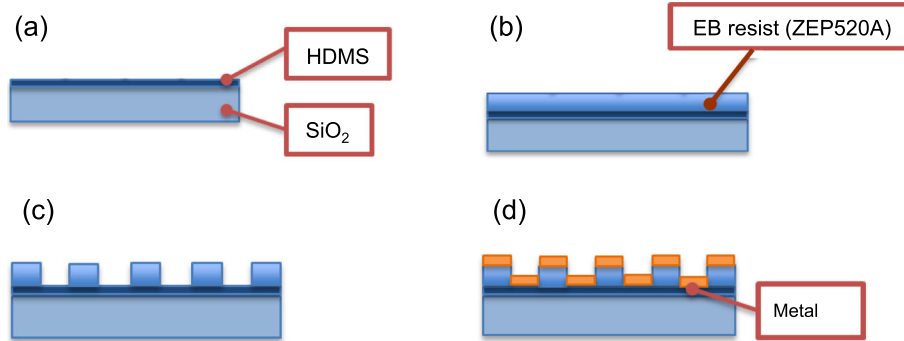


**Fig. 2** Fabrication procedure of the double-layer wire-grid structure. **a** Cleaning the  $\text{SiO}_2$  substrate and spin coating Hexamethyl disilazane. **b** Spin coating the electron-beam (EB) resist and antistatic agent. **c** Patterning using EB lithography and developing the EB resist. **d** Sputtering metal (Ag)

We performed the optical characterization using two kinds of light sources, a blue laser with a wavelength of 450 nm (CPS-450, THORLABS, output 5 mW, beam shape  $3.2 \text{ mm} \times 1.0 \text{ mm}$ , extinction ratio 25 dB) and a near-UV laser with a wavelength of 375 nm (LuxX 375–20, Omicron-Laserage Laserprodukt GmbH, output 20 mW, Beam diameter 1.5 mm, extinction ratio 20 dB). Figure 3 is a schematic of the setup for optical characterization. The laser beam, which was TM-polarized by the polarizer, was focused by a lens onto the prepared grid structure at different angles of incidence. We measured the intensity of the 0th-order diffracted patterns of the transmitted light and the reflected light using a photodiode to determine the transmittance and reflectance. We obtained the absorptance by subtracting the sum of the transmittance and the reflectance from 1.

## Results and discussion

Figure 4 shows a scanning electron microscope (SEM) image of the surface pattern fabricated using EB

lithography. In Panels (a) and (b) of this figure,  $p$  is the same (350 nm) but the duty ratio is different. Both patterns were produced according to the design values. We sputtered Ag onto this pattern to prepare the double-layer wire-grid structure.

We then performed the optical characterization using the laser beams and compared the experimental data with the simulation results. Figure 5 shows the simulated and experimental angle-of-incidence dependence of the transmittance, reflectance, and absorptance when the TM-polarized light of wavelength 450 nm is incident on a pattern with  $p = 350 \text{ nm}$  and duty ratio = 0.75. In both figures, the arrow marks the position of the absorptance peak. In the simulation, a reflectance dip can be seen at  $16.4^\circ$ , and a sharp absorptance peak occurs at the same angle. The peak absorptance is 91.2%. Note that TE-polarized light does not show such characteristics, and high reflectance is obtained in all angle ranges. Thus, the phenomenon shown in Fig. 5a occurs only for TM-polarized light. In the experiment (Fig. 5b), a peak

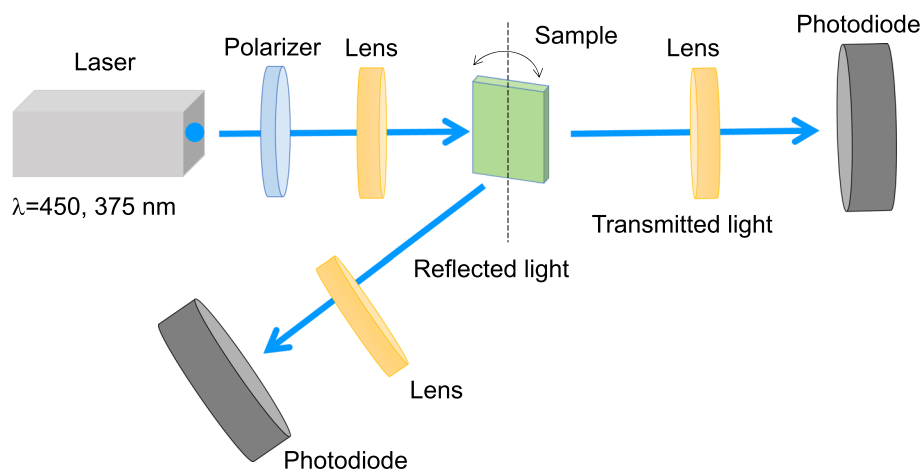


**Fig. 3** Schematic of the setup for the optical characterization. Transmittance and reflectance were measured under blue ( $\lambda = 450 \text{ nm}$ ) and near-UV ( $\lambda = 375 \text{ nm}$ ) laser light

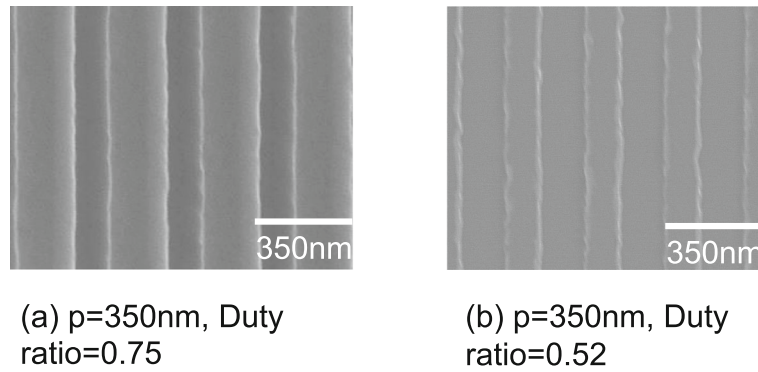


**Fig. 4** Surface SEM image of the patterns fabricated by electron-beam lithography. **a** For  $p = 350$  nm, duty ratio  $w/p = 0.75$ . **b** For  $p = 350$  nm, duty ratio  $w/p = 0.52$

absorptance of 85.4% was obtained at  $18.9^\circ$ , almost agreeing with the simulation results. The differences between the experimental and simulation results are probably explained by structural fluctuations in the fabricated structure, such as the width of the resist layer (see Fig. 4) and thickness of the Ag and resist layer.

We performed similar simulations and experiments at a wavelength of 375 nm. Figure 6 a shows the angle-of-incidence dependence of the transmittance, reflectance, and absorptance when TM-polarized light with a wavelength of 375 nm is incident on an Ag pattern with  $p = 350$  nm and duty ratio = 0.52. In the simulation, the maximum absorptance was 98.6% at a peak angle of  $4.0^\circ$ . Although the experimental results (Fig. 6b) have some additional structure, the absorptance was 95.6% at  $5.9^\circ$ , almost matching the simulation results. These results demonstrate that this

structure acts as a narrow-band perfect absorber that absorbs TM-polarized light at the specific wavelengths of 450 and 375 nm and reflects light of other wavelengths in the short-wavelength visible region and near-UV region. Perfect UV absorbers based on Al nanostructures have also been reported [42–44]. Khlopin reported an approximate absorptance of 30% in Al nanoparticle arrays [42]. Zhu reported an Al nanodisk array with a sharp absorptance of approximately 400 nm [43]. Gerasimov reported an Al nanoparticle array with 80% absorptance at 405 nm [44]. The present study achieves the approximate absorptance of 90% at 450 and 375 nm using a double-layered Ag wire-grid structure.

We then examined why an absorptance peak and a reflectance dip are obtained at a wavelength of 450 nm and an incidence angle of  $16.4^\circ$  using the reflectance

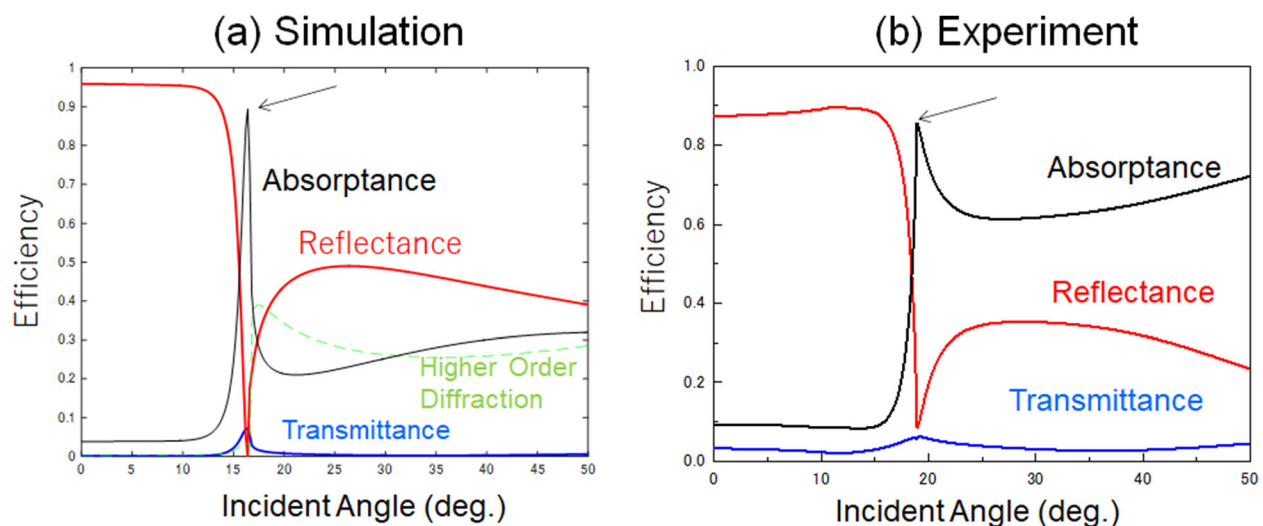
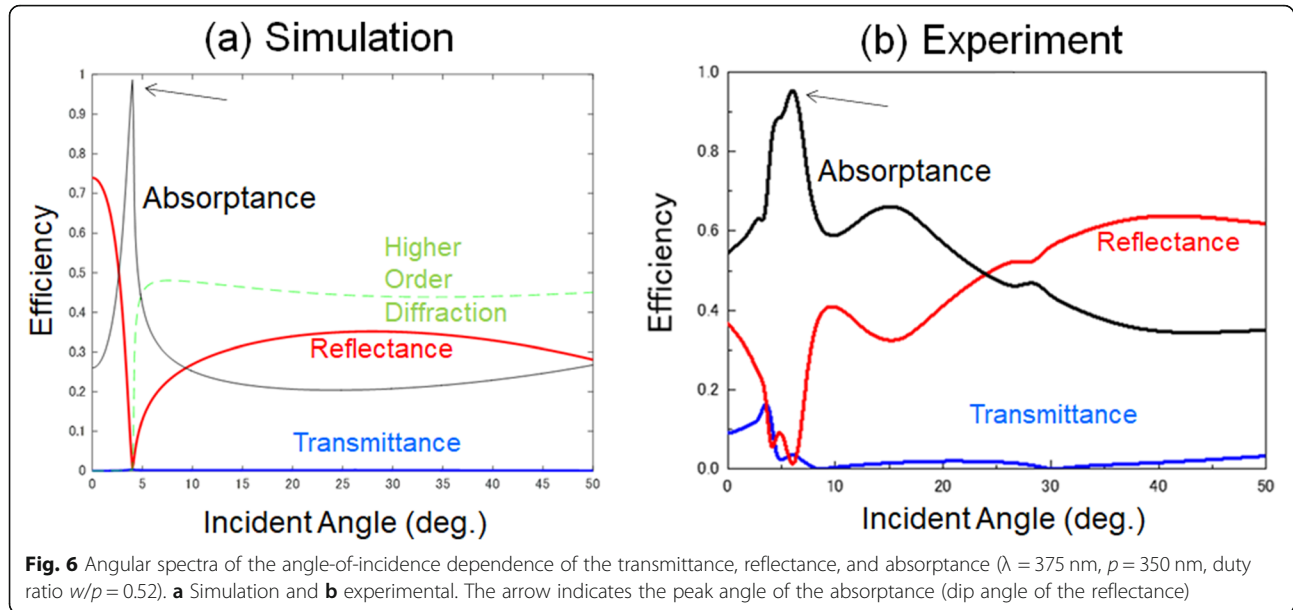
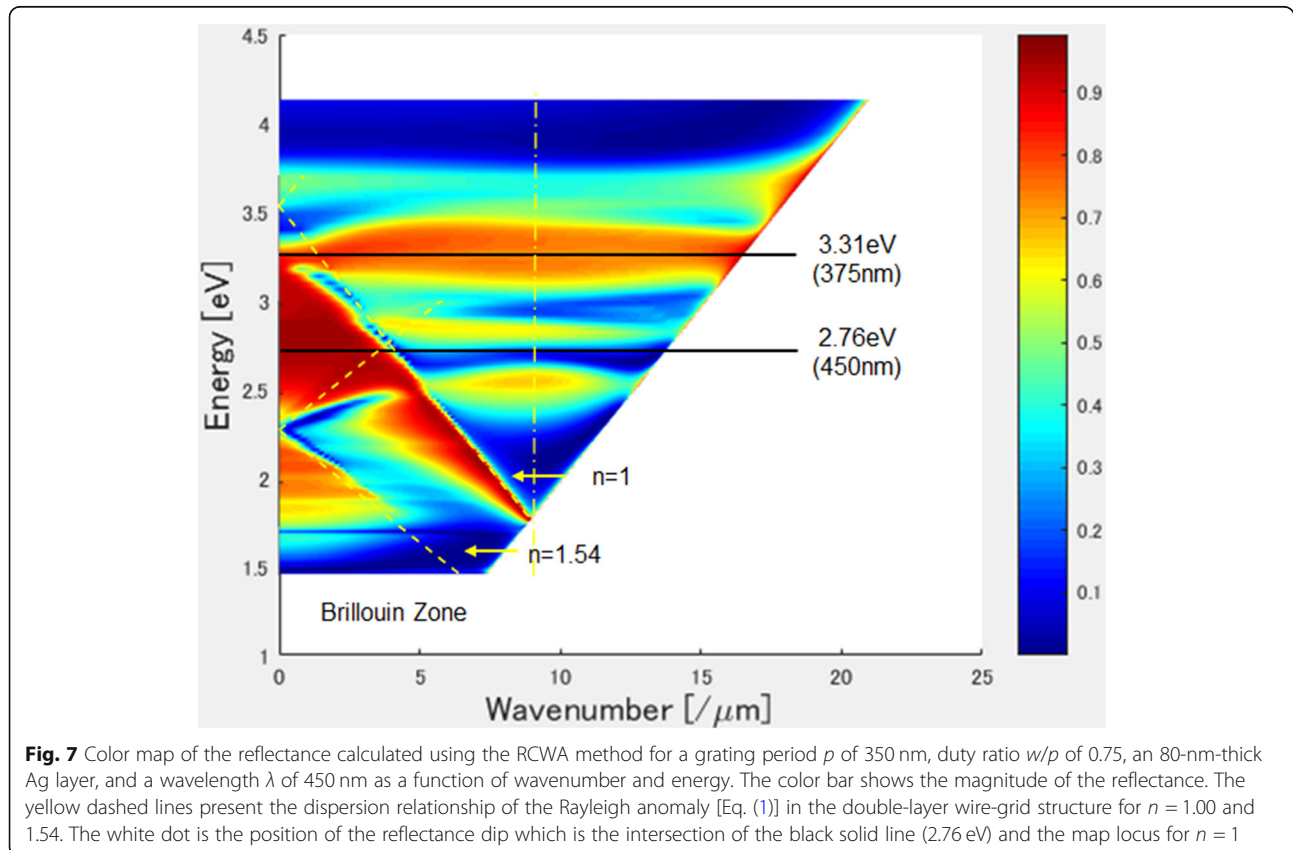


**Fig. 5** Angular spectra of the angle-of-incidence dependence of the transmittance, reflectance, and absorptance ( $\lambda = 450$  nm,  $p = 350$  nm, and duty ratio  $w/p = 0.75$ ). **a** Simulation result and **b** experimental result. The arrow indicates the peak angle of the absorptance (dip angle of the reflectance)



maps calculated by the RCWA method. Figure 7 is a color map of the reflectance for a grating period of 350 nm and a duty ratio of 0.75. The horizontal axis is the wavenumber  $k$ , the vertical axis is the energy  $\hbar\omega$ , and the color bar indicates the magnitude of the reflectance.

The solid black line corresponds to the 2.76 eV ( $\lambda = 450$  nm) and 3.31 eV ( $\lambda = 375$  nm) energies of the incident light. The blue regions in this figure represent dips in the reflectance, which correspond to the dispersion curve of the Rayleigh anomaly in the double-layer





wire-grid structure. The white dashed line is the dispersion curve of the Rayleigh anomaly [42], calculated as follows [45]:

$$\frac{\omega}{c} \sqrt{\epsilon_d} = k_0 \sin \theta + mK, \quad (1)$$

where  $\omega$ ,  $c$ , and  $k_0$  are the angular frequency, speed, and momentum of free-space light, respectively, and  $\epsilon_d$  is the relative permittivity of the adjacent dielectric material. For nonabsorbing materials,  $\epsilon_d$  can be expressed in terms of the refractive index  $n$  ( $n^2 = \epsilon_d$ ). The integer index pairs,  $m$ , denote specific SPP modes, and  $\theta$  is the excitation angle.  $K$  is the wavenumber of the diffraction grating ( $=2\pi/p$ ). These loci in the map can be fitted by Eq. (1) for  $n = 1$  and  $n = 1.54$  (yellow dashed lines in the map).

The white dot in the map is the intersection of the black solid line (2.76 eV) and the map locus for  $n = 1$ . This intersection is the position of the reflectance dip.

The angle of incidence of the light (calculated from the wavenumber) was  $16.4^\circ$ , consistent with the angle of the reflectance dip in Fig. 5a. Therefore, the large absorbance is attributable to the excitation of Rayleigh anomaly resonances in the double-layer wire-grid structure.

The resulting reflectance maps of Ag and Al at 450 and 375 nm are shown in Fig. 8. These maps relate the angle of incidence to the structural period. The several loci in these maps show the excitation conditions of the Rayleigh anomaly ( $n = 1$ , red dashed lines in Fig. 8) corresponding to the dispersion relation [42, 45]. The white dot indicates the angle of the absorbance peak. At 450 and 375 nm, the reflectance was minimized when the angle of incidence was  $16.4^\circ$  and  $4.0^\circ$ , respectively. In both the cases, the angle of minimal reflectance appeared on the loci of both Ag and Al. Therefore, in all the cases, the maximum absorbance peak and reflectance dip manifested from the excitation of the Rayleigh anomaly ( $n = 1$ ) in the double-layer wire-grid structure.

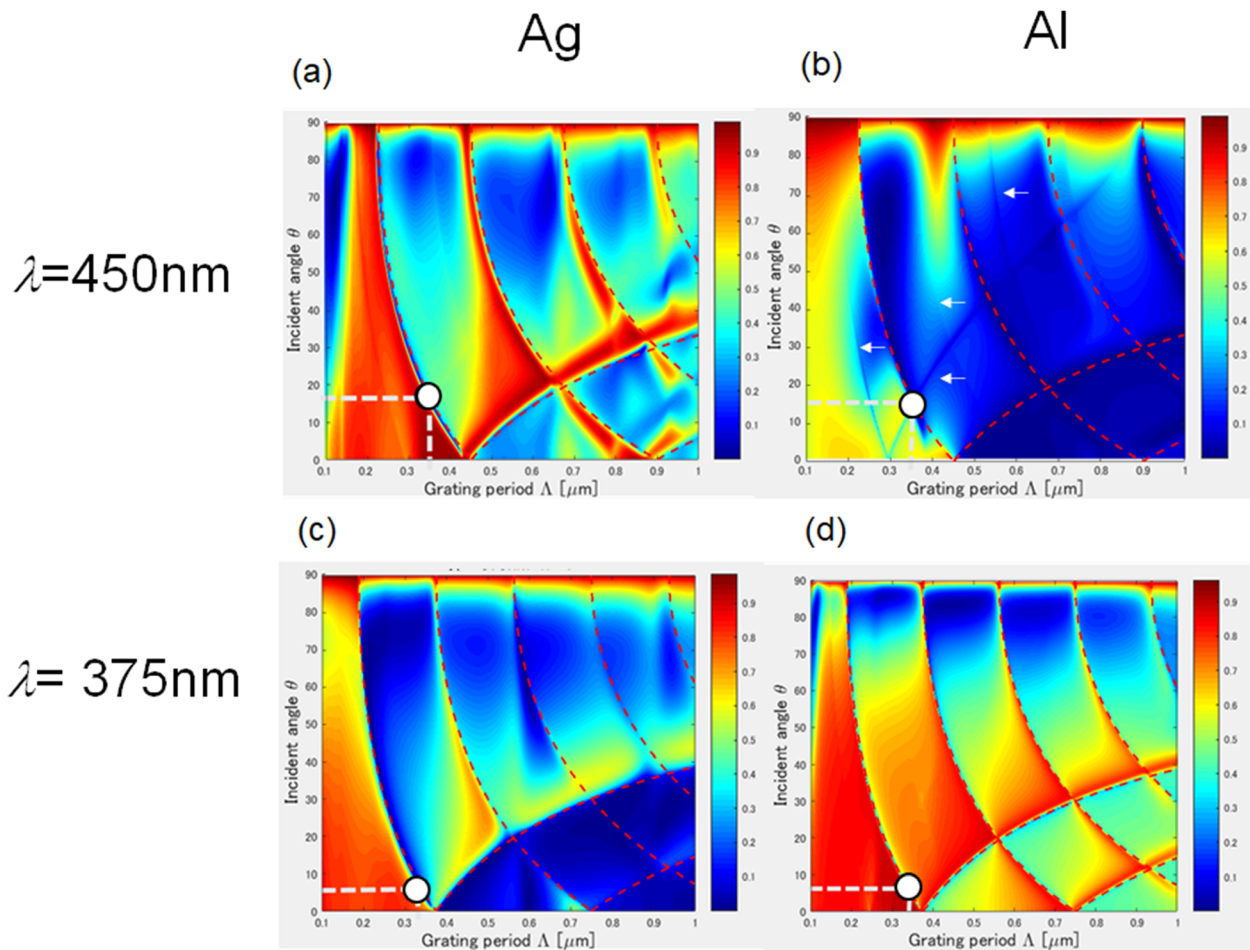


**Fig. 8** The color maps of the reflectance calculated using RCWA method. The color bar shows the magnitude of the reflectance. **a** For  $\lambda = 450$  nm, Ag. **b** For  $\lambda = 450$  nm, Al. **c** For  $\lambda = 375$  nm, Ag. **d** For  $\lambda = 375$  nm, Al. The detail structural parameter is shown in Table 1. The red dashed lines present the dispersion relationship of the Rayleigh anomaly [Eq. (1)] in the double-layer wire-grid structure for  $n = 1$ . In Panel (b), the white arrows display the dispersion relationship of the surface-plasmon polariton [Eq. (2)]

In Fig. 8 (b), the curves pointed by the white arrows cannot be fitted by the Rayleigh anomaly ( $n = 1$ ), but can be fitted by the relationship is given by Eq. (2) [45]:

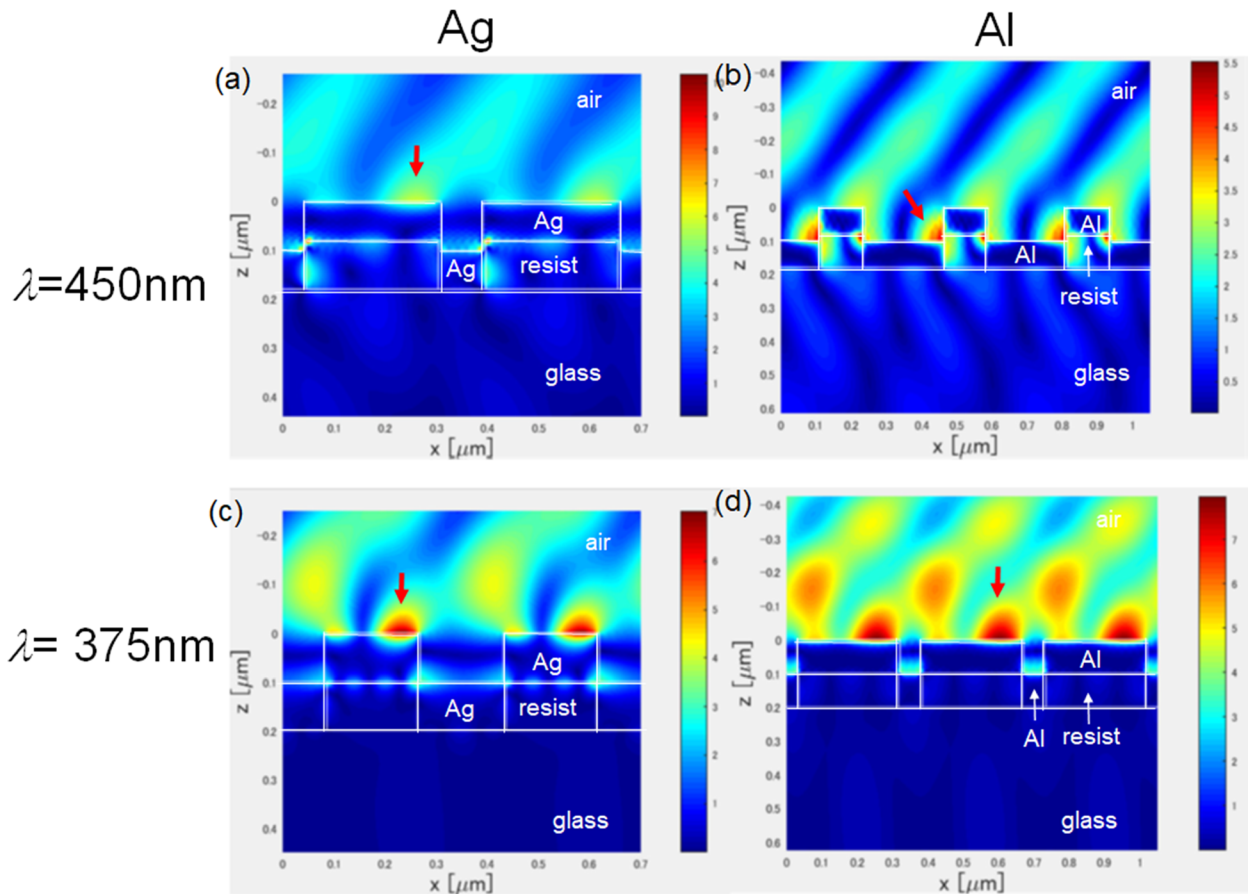
$$\frac{\omega}{c} \sqrt{\frac{\varepsilon_d \varepsilon_m}{\varepsilon_d + \varepsilon_m}} = k_0 \sin \theta + mK. \quad (2)$$

where  $\varepsilon_d = 1.45^2$  and  $\varepsilon_m$  is the relative permittivity of Al. Therefore, surface-plasmon polaritons are thought to be excited in the double-layer wire-grid structure.

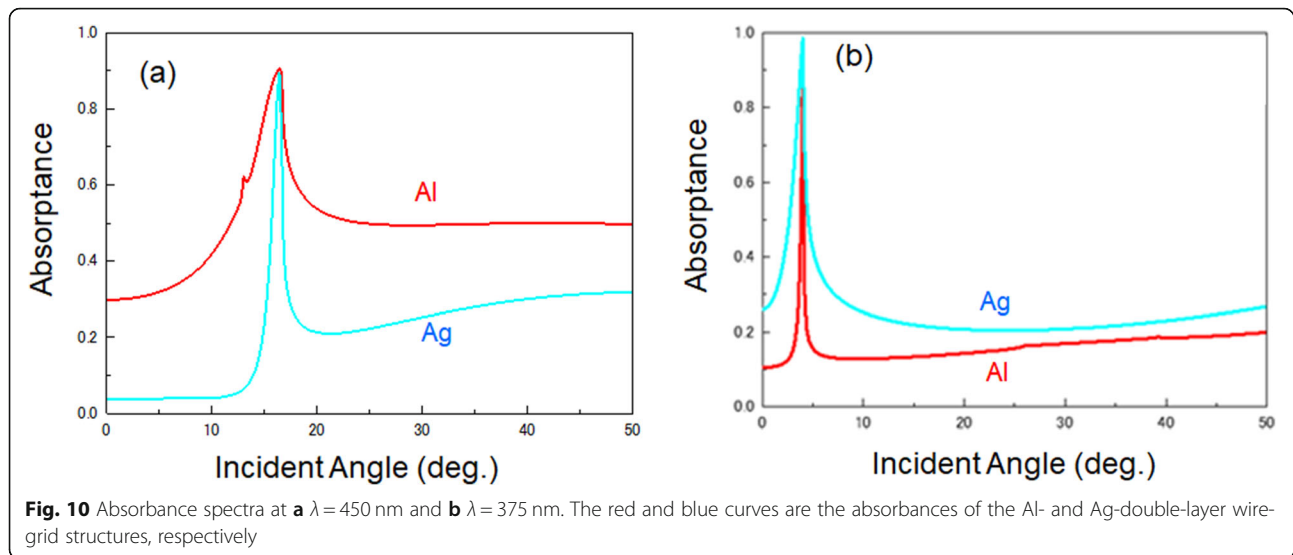
The magnetic field distributions under each condition are shown in Fig. 9. The red arrows indicate where the magnetic field is concentrated at the air–metal interface. These points correspond to the Rayleigh anomaly resonance at the air–metal interface (see Figs. 7 and 8). Therefore, the perfect absorption is probably contributed by Rayleigh anomalies at the air–metal interface.

Figure 10 compares the absorption spectra of Ag and Al. The peak angles of Ag and Al were  $16.4^\circ$  and  $4.0^\circ$ , respectively. As these absorptance-peak angles coincide

with the angles of the reflectance dips due to propagating surface-plasmon resonances, we conclude that the extraordinary absorption phenomenon are contributed by propagating surface-plasmon resonances in these systems. Such propagating resonances also explain the extraordinary transmission phenomena in double-layer wire-grid structures [33, 34]. Although both Ag and Al presented the same peak angle at both the wavelengths, the peak widths of the two metals differed at both the wavelengths. At 450 nm, Ag presented a narrower peak than Al, but this situation was reversed at 375 nm. The narrower peaks of Ag and Al at 450 and 375 nm, respectively, can be explained by the propagation lengths of the surface plasmons. After calculating the wavelength dependences of the propagation lengths of the surface-plasmon polaritons on Ag and Al, it was found that Ag has a longer propagation length ( $3.26 \mu\text{m}$ ) at 450 nm whereas Al has a longer propagation length ( $1.87 \mu\text{m}$ ) at 375 nm. Therefore, using Ag at 450 nm and Al at 375 nm, we efficiently generated propagating surface-plasmon resonances, and produced



**Fig. 9** Color maps of the distribution of the magnetic field  $H_y$  calculated using the RCWA method. The color bar shows the magnitude of the magnetic field of **a** Ag at  $\lambda = 450$  nm, **b** Al at  $\lambda = 450$  nm, **c** Ag at  $\lambda = 375$  nm, and **d** Al at  $\lambda = 375$  nm. The details of the structural parameters are given in Table 1. Red arrows indicate where the magnetic field concentrates on the interface between air and metal



sharp absorbance peaks. Therefore, we created the perfect, polarization-dependent plasmonic absorbers of short-wavelength visible light and near-UV wavelengths.

## Conclusions

In this study, we have designed a narrow-band perfect plasmonic absorber for short-wavelength visible light and the near-UV region using a double-layer wire-grid structure with Ag or Al. We simulated the angle-of-incidence dependences of the transmittance, reflectance, and absorbance, fabricated the designed structure using Ag, and compared the experimental data obtained with this structure with simulation results. At 450 and 375 nm, the maximum absorbance of Ag and Al (91.2% and 89.4%, respectively) were achieved at 16.4° and 4.0°, respectively. We thus realized a TM-polarized perfect plasmonic absorber that selectively absorbs at a specific wavelength and reflects the light of other wavelengths. We also attributed the narrow widths at the half maximum of the angular spectra of Ag at 450 nm and Al at 375 nm to differences in the propagation lengths of the surface plasmons of Ag and Al.

## Abbreviations

DC: Direct current; EB: Electron beam; RCWA: Rigorous Coupled-Wave Analysis; SEM: Scanning electron microscope; TE: Transverse electric (polarization); TM: Transverse magnetic (polarization); UV: Ultraviolet

## Acknowledgments

The authors would like to thank Prof. Takeshi Kato and Dr. Daiki Ohshima in Nagoya University for using EBL system and Prof. Yoshimasa Kawata and Prof. Wataru Inami in Shizuoka University for using UV laser. We would also thank Editage ([www.editage.jp](http://www.editage.jp)) for English language editing.

## Authors' contributions

AM is the corresponding author for this manuscript. He performed the experiments, simulations, and discussion with RT and KH. RT is a co-author of this manuscript. He conducted the experiments and simulations under the guidance of AM and KH, and he helped to draft the manuscript. KH is a co-

author of this manuscript. He executed the development of the simulation program, performed the simulation with AM and RT, and discussed the results with AM and RT. He also helped to draft the manuscript. All authors read and approved the final manuscript.

## Funding

This work was supported by the Nanotechnology Platform Program of the MEXT, Japan, Grant Number JPMXP09F19NU0018, JSPS KAKENHI, Grant Number 20 K05359, Foundation of Public Interest of Tatamatsu.

## Availability of data and materials

The datasets generated during and/or analyzed during the current study are available from the corresponding author on reasonable request.

## Declarations

## Competing interests

The authors declare that they have no competing interests.

Received: 31 December 2020 Accepted: 4 April 2021

Published online: 20 April 2021

## References

1. Tittl, A., Leitis, A., Liu, M., Yesilkoy, F., Choi, D.Y., Neshev, D.N., Yuri, S.K., Altug, H.: Imaging-based molecular barcoding with pixelated dielectric metasurfaces. *Science*. **360**, 1105–1109 (2018). <https://doi.org/10.1126/Science.aas9768>
2. Ishikawa, A., Tanaka, T.: Metamaterial absorbers infrared detection of molecular self-assembled monolayers. *Sci. Rep.* **5**(1), 12570 (2015). <https://doi.org/10.1038/srep12570>
3. Miwa, K., Ebihara, H., Fang, X., Kubo, W.: Photo-thermoelectric conversion of plasmonic nanohole array. *Appl. Sci.* **10**(8), 2681 (2020). <https://doi.org/10.3390/app10082681>
4. Tong, J.K., Hsu, W.C., Huang, Y., Boriskina, S.V., Chen, G.: Thin-film 'thermal wall' emitters and absorbers for high-efficiency thermophotovoltaics. *Sci. Rep.* **5**(1), 10661 (2015). <https://doi.org/10.1038/srep10661>
5. Rephaeli, E., Fan, S.: Absorber and emitter for solar thermophotovoltaic systems to achieve efficiency exceeding the Shockley-Queisser limit. *Opt. Exp.* **17**(17), 15145–15159 (2009). <https://doi.org/10.1364/OE.17.015145>
6. Wu, D., Liu, C., Xu, Z., Liu, Y., Yu, L., Chen, L., Li, R., Ma, R., Ye, H.: The design of ultra-broadband selective near perfect absorber based on photonic structures to achieve near-ideal daytime radiative cooling. *Mater. Des.* **139**, 104–111 (2018). <https://doi.org/10.1016/j.matdes.2017.10.1077>
7. Amemiya, K., Koshikawa, H., Imbe, M., Yamaki, T., Shitomi, H.: Perfect blackbody sheets from nano-perforated microtextured elastomers for light



- and thermal radiation management. *J. Mater. Chem. C*. **7**(18), 5418–5425 (2019). <https://doi.org/10.1039/c8tc06593d>
8. Rephaeli, E., Raman, A., Fan, S.: Ultrabroadband photonic structures to achieve high-performance daytime radiative cooling. *Nano Lett.* **13**(4), 1457–1461 (2013). <https://doi.org/10.1021/nl4004283>
  9. Rustami, E., Sasagawa, K., Sugie, K., Ohta, Y., Haruta, M., Noda, T., Tokuda, T., Ohta, J.: Needle-type image sensor with band-pass composite emission filter and parallel fiber-coupled laser excitation. *IEEE Trans. Circuits Syst.-I*. **67**(4), 1082–1091 (2020). <https://doi.org/10.1109/TCSI.2019.2959592>
  10. Okamoto, K., Okura, K., Wang, P., Ryuzaki, S., Tamada, K.: Flexibly tunable surface plasmon resonance by strong mode coupling using a random metal nanohemisphere on mirror. *Nanophotonics*. **9**(10), 3409–3418 (2020). <https://doi.org/10.1515/nanoph-2020-0118>
  11. Liang, C.J., Huang, K.Y., Hung, L.T., Su, C.Y.: Rapidly fabrication of plasmonic structural color thin films through AAO process in an alkaline solution. *Surf. Coat. Technol.* **319**, 170–181 (2017). <https://doi.org/10.1016/j.surfcoat.2017.04.011>
  12. Ellenbogen, T., Seo, K., Crozer, K.B.: Chromatic plasmonic polarizers for active visible color filtering and polarimetry. *Nano Lett.* **12**(2), 1026–1031 (2012). <https://doi.org/10.1021/nl204257g>
  13. Xu, T., Wu, Y.K., Luo, X., Guo, L.J.: Plasmonic nanoresonators for high resolution colour filtering and spectral imaging. *Nat. Commun.* **1**(1), 59 (2010). <https://doi.org/10.1038/ncomms1058>
  14. Yokogawa, S., Burgos, S., Atwater, H.A.: Plasmonic color filters for CMOS image sensor applications. *Nano Lett.* **12**(8), 4349–4354 (2012). <https://doi.org/10.1021/nl302110z>
  15. Chen, Q., Cumming, D.R.S.: High transmission and low color cross-talk plasmonic color filters using triangular-lattice hole arrays in aluminum films. *Opt. Exp.* **18**(13), 14056–14062 (2010). <https://doi.org/10.1364/OE.18.014056>
  16. Mazulquim, D.B., Lee, K.J., Yoon, J.W., Muniz, L.V., Borges, B.-H.V., Neto, L.G., Magnusson, R.: Efficient band-pass color filters enabled by resonant modes and plasmons near the Rayleigh anomaly. *Opt. Exp.* **22**(25), 30843–30851 (2014). <https://doi.org/10.1364/OE.22.030843>
  17. Tan, J., Wu, Z., Xu, K., Meng, Y., Jin, G., Wang, L., Wang, Y.: Numerical study an au-ZnO-Al absorber for a color filter with a high quality factor. *Plasmonics*. **15**(1), 293–299 (2020). <https://doi.org/10.1007/s11468-019-01047-z>
  18. Ghobadi, A., Hajian, H., Soydan, M.C., Butun, B., Ozbay, E.: Lithography-free planar band-pass reflective color filter using a series connection of cavities. *Sci. Rep.* **9**(1), 220 (2019). <https://doi.org/10.1038/s41598-018-36540-8>
  19. Li, W., Valentine, J.: Metamaterial perfect absorber based hot electron photodetection. *Nano Lett.* **14**(6), 3510–3514 (2014). <https://doi.org/10.1021/nl501090w>
  20. Zhao, X., Yang, Y., Wang, Y., Hao, Y., Chen, Z., Zhang, M.: Study of the converter based on photonic crystals filters and quantum dots for solar blind ultraviolet imaging system. *Opt. Eng.* **57**(11), 117106 (2018). <https://doi.org/10.1117/1.OE.57.11.117106>
  21. Hennesy, J., Jewell, A.D., Hoenk, M.E., Nikzad, S.: Metal-dielectric filters for solar-blind silicon ultraviolet detectors. *Appl. Opt.* **54**(11), 3507–3512 (2015). <https://doi.org/10.1364/AO.54.11.003507>
  22. Li, X., Xu, J.: Synthesis of CdS QDs with single cubic and hexagonal lattice for blue-light-blocking nanocomposite films with a narrow absorbing transitional band. *Mater. Today Commun.* **24**, 101108 (2020). <https://doi.org/10.1016/j.mtcomm.2020.101108>
  23. Liu, N., Mesch, M., Weiss, T., Hentschel, M., Giessen, H.: Infrared perfect absorber and its application as plasmonic sensor. *Nano Lett.* **10**(7), 2342–2348 (2010). <https://doi.org/10.1021/nl9041033>
  24. Ding, F., Jin, Y., Li, B., Cheng, H., Mo, L., He, S.: Ultrabroadband strong light absorption based on thin multilayered metamaterials. *Laser Photon. Rev.* **8**(6), 946–953 (2014). <https://doi.org/10.1002/lpor.201400157>
  25. Hao, J., Wang, J., Liu, X., Padilla, W.J., Zhou, L., Qiu, M.: High performance optical absorber based on a plasmonic metamaterial. *Appl. Phys. Lett.* **96**(25), 251104 (2010). <https://doi.org/10.1063/1.3442904>
  26. Ding, F., Yang, Y., Deshpande, R.A., Bozhevolnyi, S.I.: A review of gap-surface plasmon metasurfaces: fundamentals and applications. *Nanophotonics*. **7**(6), 1129–1156 (2018). <https://doi.org/10.1515/nanoph-2017-0125>
  27. Hu, J., Shen, M., Li, Z., Li, X., Liu, G., Wang, X., Kan, C., Li, Y.: Dual-channel extraordinary ultraviolet transmission through an aluminum nanohole array. *Nanotechnology*. **28**(21), 215205 (2017). <https://doi.org/10.1088/1361-6528/aa6a38>
  28. Li, W.D., Chou, S.Y.: Solar-blind deep-UV band filter (250–350 nm) consisting of a metal nano-grid fabricated by nanoimprint lithography. *Opt. Exp.* **18**(2), 931–937 (2010). <https://doi.org/10.1364/OE.18.000931>
  29. Jakšić, Z., Maksimović, M., Sarajlić, M., Tanasković, D.: Surface plasmon-polariton assisted metal-dielectric multilayers as passband filters for ultraviolet range. *Acta Physica Polonica A*. **112**, 953–958 (2007). <https://doi.org/10.12693/APhysPolA.112.953>
  30. Mu, J., Lin, P.T., Zhang, L., Michel, J., Kimerling, L.C., Jaworski, F., Agarwal, A.: Design and fabrication of a high transmissivity metal-dielectric ultraviolet band-pass filter. *Appl. Phys. Lett.* **102**(21), 213105 (2013). <https://doi.org/10.1063/1.4807925>
  31. Morsy, A.M., Povinelli, M.L., Hennessy, J.: Highly selective ultraviolet aluminum plasmonic filters on silicon. *Opt. Exp.* **26**(18), 22650–22657 (2018). <https://doi.org/10.1364/OE.26.022650>
  32. Gao, H., Peng, W., Cui, W., Chu, S., Yu, L., Yang, X.: Ultraviolet to near infrared titanium nitride broadband plasmonic absorber. *Opt. Mater.* **97**, 109377 (2019). <https://doi.org/10.1016/j.optmat.2019.109377>
  33. Ghobadi, A., Hajian, H., Butun, B., Ozbay, E.: Strong light-matter interaction in lithography-free planar metamaterial perfect absorbers. *ACS Photonics*. **5**(11), 4203–4221 (2018). <https://doi.org/10.1021/acsphotonics.8b00872>
  34. Hajian, H., Ghobadi, A., Butun, B., Ozbay, E.: Active metamaterial nearly perfect light absorbers: a review. *J. Opt. Soc. Am. B*. **36**(8), F131–F143 (2019). <https://doi.org/10.1364/JOSAB.36.00F131>
  35. Feng, L., Huo, P., Liang, Y., Xu, T.: Photonic metamaterial absorbers: morphology engineering and interdisciplinary applications. *Adv. Mater.* **32**, 1903787 (2020). <https://doi.org/10.1002/adma.201903787>
  36. Ng, C., Wesmann, L., Pachenko, E., Song, J., Davis, T.J., Roberts, A., Gómez, D.E.: Plasmonic near-complete optical absorption and its applications. *Adv. Opt. Mater.* **7**(14), 1801660 (2018). <https://doi.org/10.1002/adom.201801660>
  37. Motogaito, A., Morishita, Y., Miyake, H., Hiramatsu, K.: Extraordinary optical transmission exhibited by surface plasmon polaritons in a double-layer wire grid polarizer. *Plasmonics*. **10**(6), 1657–1662 (2015). <https://doi.org/10.1007/s11468-015-9980-8>
  38. Motogaito, A., Nakajima, T., Miyake, H., Hiramatsu, K.: Excitation mechanism of surface plasmon polaritons in a double-layer wire grid structure. *Appl. Phys. A Mater. Sci. Process.* **123**(12), 729 (2017). <https://doi.org/10.1007/s00339-017-1367-6>
  39. Motogaito, A., Mito, S., Miyake, H., Hiramatsu, K.: Detecting high-refractive-index media using surface plasmon sensor with one-dimensional metal diffraction grating. *Opt. Photon. J.* **6**(07), 164–170 (2016). <https://doi.org/10.4236/opj.2016.67018>
  40. Motogaito, A., Ito, Y.: Excitation mechanism of surface plasmon polaritons for surface plasmon sensor with 1D metal grating structure for high refractive index medium. *Photon. Sens.* **9**(1), 11–18 (2019). <https://doi.org/10.1007/s13320-018-0515-8>
  41. Motogaito, A., Watanabe, A.: Wave plate fabrication using surface plasmon polariton in a Ag wire grid structure. Technical digest on the 24th Microoptics Conference, pp. 250–251 (2019). <https://doi.org/10.23919/MOC4.6630.2019.8982793>
  42. Khlopin, D., Laux, F., Wardley, W.P., Martin, J., Wurtz, G.A., Plain, J., Bonod, N., Zayats, A.V., Dickson, W., Gérard, D.: Lattice modes and plasmonic linewidth engineering in gold and aluminum nanoparticle arrays. *J. Opt. Soc. Am. B*. **34**(3), 691–700 (2017). <https://doi.org/10.1364/JOSAB.34.000691>
  43. Zhu, X., Hossain, G.M.I., George, M., Farhang, A., Cicek, A., Yanik, A.A.: Beyond noble metals: high Q-factor aluminum nanoplasmonics. *ACS Photon.* **7**(2), 416–424 (2020). <https://doi.org/10.1021/acsphotonics.9b01368>
  44. Gerasimov, V.S., Ershov, A.E., Bikbaev, R.G., Rasskazov, I.L., Isaev, I.L., Semina, P. N., Kostyukov, A.S., Zakomirnyi, V.I., Polyutov, S.P., Karpov, S.V.: Plasmonic lattice Kerker effect in ultraviolet-visible spectral range. *Phys. Rev. B*. **103**(3), 035402 (2021). <https://doi.org/10.1103/PhysRevB.103.035402>
  45. Gao, H., McMahon, J.M., Lee, M.H., Henzie, J., Gray, S.K., Schatz, G.C., Odom, T. W.: Rayleigh anomaly-surface plasmon polariton resonances in palladium and gold subwavelength hole arrays. *Opt. Exp.* **17**(4), 2334–2340 (2009). <https://doi.org/10.1364/OE.17.002334>

## Publisher's Note

Springer Nature remains neutral with regard to jurisdictional claims in published maps and institutional affiliations.